

# Personalized 4D Whole-Heart Mesh Reconstruction from Cine MRI via Multi-Scale Temporal Modeling and Differentiable Contour Rendering

Xiaoyue Liu<sup>a</sup>, Dongcheng Cang<sup>a</sup>, Xiaohan Yuan<sup>a,b</sup>, Mark YY Chan<sup>c,d</sup>, Ching-Hui Sia<sup>c,d</sup>, Lei Li<sup>\*a</sup>

<sup>a</sup>Department of Biomedical Engineering, National University of Singapore, Singapore

<sup>b</sup>School of Automation, Southeast University, Nanjing, China

<sup>c</sup>Department of Medicine, National University of Singapore, Singapore

<sup>d</sup>Department of Cardiology, National University Heart Centre Singapore, Singapore

---

## Abstract

Accurate 4D whole-heart mesh reconstruction from sparse cine MRI is critical for creating cardiac digital twins, but remains challenging due to limited 2D slice coverage and the complex coupling between cardiac shape and motion. Existing methods often rely on intermediate contour fitting and typically reconstruct static, single-phase, or partial cardiac geometries, limiting their ability to capture full-chamber dynamics. We propose a novel end-to-end framework for reconstructing temporally resolved whole-heart meshes from multi-view 2D cine MRI sequences by learning an image-to-mesh mapping. The framework incorporates a differentiable contour renderer inspired by the Beer-Lambert attenuation principle, enabling anatomy-aware supervision of 3D+t mesh deformation through contour-based projection losses. To improve temporal consistency across the cardiac cycle, we further introduce a multi-scale temporal modeling module that integrates global cycle-level dynamics with local inter-frame coherence to generate smooth and physiologically plausible mesh trajectories. The proposed method achieved a whole-heart mean absolute error of  $1.68 \pm 0.31$  mm and a motion jitter of  $0.77 \pm 0.17$  mm/frame<sup>3</sup>, outperforming existing methods with lower reconstruction error and substantially improved motion smoothness. It also improved 2D contour alignment across multiple cine MRI views and supported downstream proof-of-concept electrophysiological simulation. The code will be released publicly upon acceptance of the manuscript for publication.

**Keywords:** 4D Whole Heart Reconstruction, Cine MRI, Multi-Scale Temporal Modeling, Differentiable Rendering, Cardiac Digital Twin

---

## 1. Introduction

Cardiovascular diseases remain the leading cause of mortality worldwide, making reliable assessment of cardiac structure and function essential for clinical diagnosis and therapeutic decision-making (Chong et al., 2025). In this context, cardiac digital twin (CDT) technology has emerged as a powerful tool for creating patient-specific virtual heart models, enabling real-time visualization and analysis of the heart (Li et al., 2024a). By offering detailed insights into the underlying mechanisms of the heart, CDT has the potential to revolutionize cardiac diagnosis and treatment (Corral-Acero et al., 2020; Arevalo et al., 2016). A typical CDT workflow consists of two key stages: anatomical twinning and functional twinning (Gillette et al., 2021; Li et al., 2024b). Anatomical twinning involves extracting 3D heart geometry from images and identifying pathological regions when present. Considering the dynamic nature of cardiac motion, 4D (3D+t) geometry is typically required for a more comprehensive representation. Cine MRI can be used for this purpose, as it provides non-invasive

visualization of cardiac anatomy and motion throughout the cardiac cycle. However, cine MRI typically acquires sparse and intersecting 2D image planes, i.e., short-axis (SAX) and long-axis (LAX) slices, leaving substantial spatial gaps that make accurate 4D cardiac geometry reconstruction highly challenging.

Conventional cine MRI based cardiac geometry reconstruction frameworks therefore generally consist of two steps, i.e., image segmentation, followed by mesh generation based on contours derived from the segmentation (Gaggion et al., 2025). This is mainly because direct volumetric reconstruction from cine MRIs is challenging due to the inherent sparsity and anisotropy of the data. By first segmenting the cardiac structures, the extracted contours can serve as geometric constraints to guide the mesh generation. Nevertheless, traditional iso-surfacing algorithms, such as marching cubes, struggle to generate smooth and anatomically accurate meshes due to the irregular spacing and insufficient volumetric information in the input data. To solve this, many previous studies employed mesh adaptation approaches, such as template mesh deformation (Villard et al., 2018; Hu et al., 2023), statistical shape model (SSM) (Banerjee et al., 2021), and B-spline sur-

---

URL: [lei.li@nus.edu.sg](mailto:lei.li@nus.edu.sg) (Lei Li\*)

face reconstruction (Odille et al., 2018). Furthermore, image interpolation based methods have also been applied to reconstruct high-resolution 3D geometry (Ukwatta et al., 2015). However, these techniques are labor-intensive and time-consuming, which significantly hinders their feasibility for real-time applications.

Recently, deep learning based methods have shown promising performance for efficient 3D cardiac geometry reconstruction (Yuan et al., 2023; Gaggion et al., 2025). Similar to the conventional pipeline, these deep learning based methods generally rely on pre-generated segmentation and then directly convert sparse contours into 3D meshes via point/ shape completion network (Beetz et al., 2023; Ma et al., 2025), flow matching (Ma et al., 2026), or graph convolution network based template deformation (Chen et al., 2021; Ye et al., 2023). Furthermore, most studies focus only on partial cardiac anatomy, such as the left ventricular (LV) myocardium (Joyce et al., 2022; Yuan et al., 2023; Meng et al., 2023) or the biventricular model (Chen et al., 2021; Beetz et al., 2023), reducing their applicability to whole-heart functional twinning. Other approaches that achieve whole-heart reconstruction rely on high-resolution volumetric CT or MRI data (Kong and Shadden, 2022), which are not part of standard clinical workflows. Most critically, recent frameworks that reconstruct from sparse 2D cine MRI primarily operate on static 3D shape at isolated cardiac phases (Gaggion et al., 2025; Ma et al., 2025). They failed to model the continuous temporal dynamics and the intrinsic coupling of cardiac shape and motion throughout the cycle. This omission limits the physiological fidelity required for dynamic simulations. In general, these work either rely on high-resolution volumetric images or solely reconstructed part of the whole heart or single phase of the heart.

In this study, we introduce a novel framework that reconstructs temporally resolved whole-heart meshes directly from sparse multi-view cine MRI by jointly learning shape and motion information. Given multi-view cine MRIs, the model can efficiently learn an image-to-mesh mapping between cine MRI representations and mesh deformation space. Specifically, we utilize the domain-specific autoencoder networks to extract the compact latent representations of both cine MRIs and the mesh sequences. Then, the mapping between the image and heart mesh sequences latent spaces can be learned to ensure the generated shapes align with the mesh deformation space. This study is a systematic extension of our previous conference work (Liu et al., 2026). We provide more comprehensive quantitative functional evaluation, including quantitative assessment of ejection fraction and chamber volume. We also include external validation on the public dataset to assess cross-domain generalizability. More importantly, we demonstrate the feasibility of using the reconstructed whole-heart meshes as anatomical substrates for downstream in-silico electrophysiological (EP) simulation. The main contributions of this work include:

- i. We present a novel end-to-end image-to-mesh pipeline that reconstructs patient-specific 4D whole-heart meshes directly from multi-view 2D cine MRI sequences.
- ii. We design a physics-inspired differentiable rendering loss, based on the Beer–Lambert law, which leverages multi-view 2D+t segmentation contours as direct supervision for 3D+t mesh reconstruction.
- iii. We develop a multi-scale temporal modeling module that models high-dimensional image-sequence dynamics to produce a smooth and physiologically plausible latent trajectory for 4D mesh generation.
- iv. We demonstrate the feasibility of using reconstructed whole-heart meshes for proof-of-concept EP simulation, supporting their potential integration into CDT workflows.

## 2. Related Work

### 2.1. 3D Cardiac Reconstruction from Sparse 2D Medical Imaging

Reconstructing patient-specific 3D anatomy from sparse 2D observations is a persistent problem in cardiac image analysis across different modalities including echocardiography (echo), X-ray angiography, and MRI (Sarmah et al., 2023). In echo, limited acoustic windows yield only a few intersecting 2D planes, from which the complete 3D cardiac anatomy must be inferred despite poor boundary visibility and speckle artifact (Laumer et al., 2025; Yu et al., 2025). In biplane X-ray angiography, two near-orthogonal projections are used to reconstruct coronary vessel geometry, relying on epipolar constraints and vesselness priors to resolve depth ambiguity (Bransby et al., 2023). In sparse-slice MRI, where only a small number of slices are acquired, reconstructing complete anatomical surfaces requires strong regularization to fill unsampled regions (Ukwatta et al., 2015). Despite differences in imaging physics, these tasks share the challenge of reconstructing complete 3D anatomy from partial, view-dependent observations.

Traditional approaches for reconstructing cardiac anatomy from sparse 2D cine MRI generally follow a segmentation-to-shape pipeline, where SAX and LAX images are first converted into intermediate contours or shape observations and then used to fit statistical shape models (Ukwatta et al., 2015), deform template meshes (Odille et al., 2018), or construct spline-based surfaces (Banerjee et al., 2021). Although these methods provide explicit geometric constraints, their reconstruction quality depends heavily on hand-crafted shape fitting. More recent learning-based methods have introduced data-driven components into this pipeline, including volume super-resolution (Oktay et al., 2017), point-to-mesh prediction (Ye et al., 2023), and shape deformation (Xiao et al., 2024; Chen et al.,

2021). However, many of these methods still rely on intermediate segmentations, contours, regular-grid representations, or point-cloud inputs, rather than directly reconstructing complete anatomical meshes from sparse multi-view cine MRI. Moreover, most approaches only focus on one or two ventricular structures (Chen et al., 2021; Beetz et al., 2021), providing an incomplete representation of the whole heart. Also, many learning based models rely on simulated SAX and LAX MRI slices from 3D images for training, which may limit their adaptability to real 2D cine MRI (Beetz et al., 2021; Chen et al., 2021; Xu et al., 2023).

## 2.2. Cardiac Motion Modeling and Analysis

Cardiac motion analysis is fundamental for evaluating cardiac function and characterizing abnormal mechanical behavior (Yu et al., 2014). Recovering myocardial deformation and chamber dynamics enables quantitative assessment of ejection fraction (Ouyang et al., 2020), strain (López et al., 2023), and other clinically relevant biomarkers that support diagnosis, risk stratification, and treatment planning (Bello et al., 2019). Different imaging modalities offer complementary strengths for motion analysis. Echo provides high temporal resolution and broad clinical accessibility, with motion estimation typically performed by tracking speckle or intensity patterns, though challenges remain in out-of-plane motion handling and signal dropout (Evain et al., 2022; Ouyang et al., 2020). Tagged MRI embeds explicit magnetic tag patterns into the myocardium, allowing precise tracking of tissue displacement and strain across the cardiac cycle, though its specialized acquisition limits routine use (Wang et al., 2019). In routine clinical practice, cine MRI is more commonly available than tagged MRI, offering dynamic anatomical information without specialized sequences (Bello et al., 2019; López et al., 2023).

Depending on the representation, cine-based methods may estimate motion at the image, point cloud, or mesh level. At the image level, cine MRI motion tracking is commonly formulated as dense frame-to-frame or full-cycle motion estimation, either through registration-based alignment or optical-flow-based displacement recovery. Traditional registration methods recover cine MRI motion by spatially aligning image frames and estimating deformation fields under regularization or physical constraints (Bischoff et al., 2008; Qiao et al., 2020). Optical-flow-based methods estimate cine MRI motion as dense pixel-wise displacement fields from local image correspondences or learned apparent-flow representations (Wang et al., 2019; Zheng et al., 2019). Although image-level cine motion tracking can estimate dense pixel-wise displacement fields, it does not directly provide explicit anatomical surface trajectories or mesh-based geometric measurements such as vertex-wise correspondence, chamber-wise deformation, and time-resolved surface geometry (Meng et al., 2022, 2023). At the point-cloud level, cine-based cardiac motion modeling represents reconstructed cardiac surfaces as

unordered 3D point sets and estimates anatomical deformation between cardiac phases. For example, point-cloud deformation has been used to model biventricular contraction and relaxation between end-diastolic and end-systolic phases from cine-derived cardiac point clouds (Beetz et al., 2024). However, because point clouds are unordered, they lack explicit surface connectivity and fixed vertex correspondence, which limits their direct use for topology-preserving cardiac surface motion tracking (Lemeunier et al., 2022). Among these, mesh-based motion reconstruction is particularly attractive because it preserves anatomical correspondence over time and enables direct analysis of chamber deformation, myocardial motion, and subject-specific functional biomarkers (Lyu et al., 2026; Yang et al., 2026). Single-chamber mesh modeling has been explored by Joyce et al. (2022), who fitted personalized LV meshes to sparse cine MRI slices throughout the cardiac cycle to derive functional measurements specific to the LV such as volume and strain. A representative biventricular approach is DeepMesh, which estimates 3D cardiac mesh motion from multi-view cine MRI and preserves vertex correspondence across frames for ventricular motion analysis (Meng et al., 2023). However, single- or biventricular mesh tracking only provides a partial representation of cardiac dynamics, limiting its ability to capture coordinated motion across the whole heart. Recently, Ma et al. (2026) attempted to synthesize whole-heart cardiac motion using flow matching. Such synthesis-based methods mainly generate plausible motion patterns rather than reconstructing patient-specific anatomical dynamics directly constrained by cine MRI observations.

## 2.3. Whole-Heart Simulation for Cardiac Digital Twins

Digital twins have emerged as a powerful paradigm for personalized medicine, enabling *in silico* prediction of patient-specific cardiac function, treatment response, and disease progression (Corral-Acero et al., 2020; Arevalo et al., 2016). However, the majority of existing cardiac simulation studies have focused on isolated chambers, most commonly the ventricles, reflecting the relative maturity and clinical importance of ventricular modeling (Gillette et al., 2021; Li et al., 2024b, 2025). Atrial-only simulations, while increasingly studied in the context of arrhythmias such as atrial fibrillation, typically neglect atrioventricular coupling and the mechanical influence of ventricular contraction on atrial dynamics (Zappon et al., 2025; Boyle et al., 2019). Conversely, ventricular-only models often ignore the atria altogether, treating them as passive pressure boundary conditions or omitting them entirely. This compartmentalized approach fails to capture physiologically important atrioventricular interactions (Fedele et al., 2023). The gap persists because the atria exhibit thin-walled, complex trabeculated anatomy and are physiologically coupled to ventricular dynamics, making their inclusion computationally demanding and data-intensive. Furthermore, personalizing whole-heart models requires

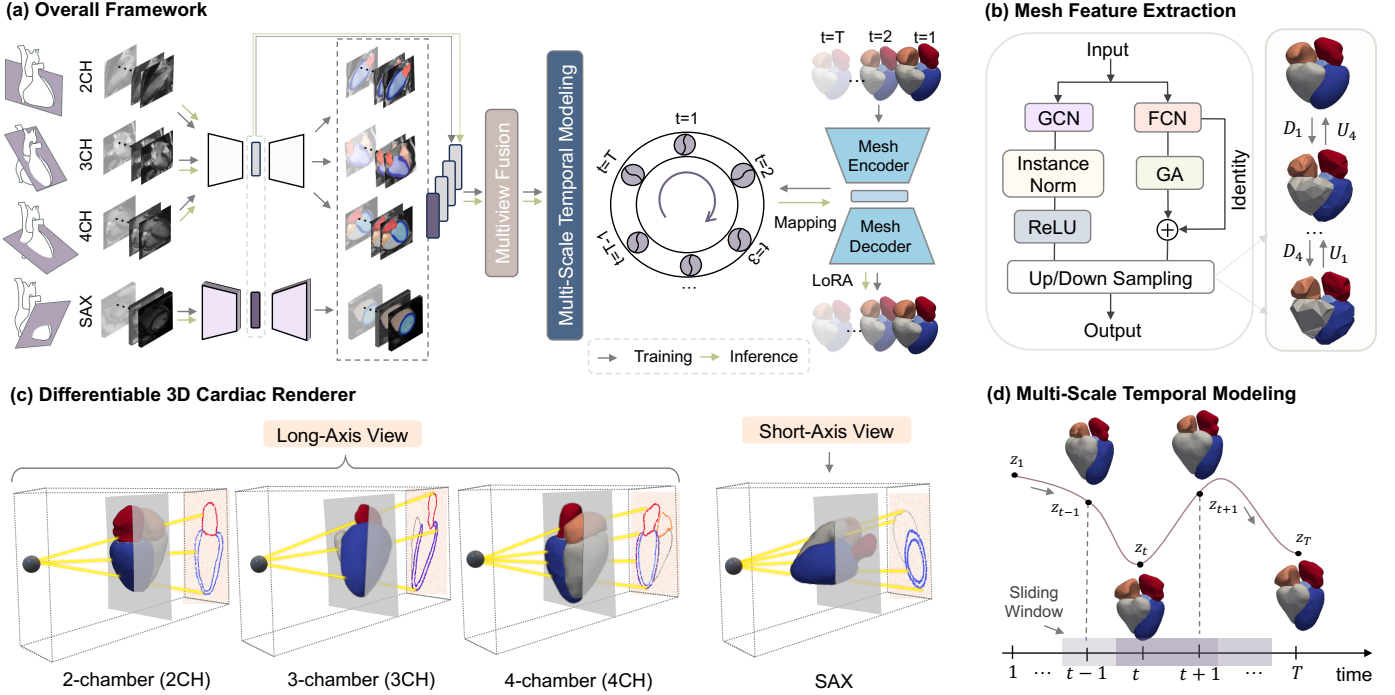


Figure 1: Illustration of the proposed multi-view cine-MRI based 4D whole heart mesh reconstruction framework. GCN: graph convolutional network; 2/ 3/ 4CH: 2/ 3/ 4-chamber; SAX: short-axis; FCN: fully convolutional network; GA: graph attention; LoRA: low-rank adaptation.

anatomical reconstructions of all four chambers, tissue property estimation across heterogeneous structures, and validation against multi-chamber functional data, all of which remain nontrivial. Consequently, advancing whole-heart digital twins to fully capture atrioventricular interaction remains an essential and still-evolving frontier in personalized cardiac modeling. Recently, several studies have taken important steps toward whole-heart simulation. For instance, Fedele et al. (2023) developed a biophysically detailed electromechanical model of the whole human heart that considers both atrial and ventricular contraction, incorporating patient-specific geometry, fiber architecture, and tissue properties to simulate coupled electromechanics across all four chambers. In parallel, Gillette et al. (2022) proposed a personalized virtual model of entire organ-scale electrophysiology of all four-chambers of the heart. More recently, Salvador et al. (2024) introduced a data-driven framework using latent neural ordinary differential equations to accelerate whole-heart electromechanical simulations, achieving substantial speedups while preserving biophysical fidelity. Despite these advances, whole-heart simulation remains computationally expensive and sensitive to parameter choices. Most existing methods rely on high-resolution volumetric imaging to construct detailed patient-specific meshes, and they typically assume the availability of dense 3D geometry at a single representative time point, with motion either prescribed or simulated from first principles rather than directly inferred from routine clinical acquisitions.

### 3. Methodology

Figure 1 (a) provides an overview of the proposed 4D whole heart reconstruction model, consisting of domain-specific feature extractors and latent dynamic mapping. To achieve 4D mesh reconstruction from cine MRI, we design a cross-domain mapping module to bridge the image domain and mesh domain (Sec. 3.1). U-Net and mesh VAE networks are employed to extract the compact latent representations of cine MRIs and mesh sequences, respectively. Additionally, a multi-scale temporal modeling module is introduced to capture cycle-level cardiac dynamics and inter-frame coherence (Sec. 3.2). Then, we employ a differentiable rendering to explicitly learn the spatial relationship among the 2D(+t) sparse cardiac segmentation and 3D(+t) mesh (Sec. 3.3). Finally, Sec. 3.4 presents the details of the reconstruction model for the personalized inference of 4D whole heart mesh.

#### 3.1. Image-to-Mesh Latent Space Mapping via Anatomical Feature Alignment

For image feature extraction, we employ a pretrained cardiac U-Net (Ronneberger et al., 2015) to extract the anatomy of cardiac chambers. Given multi-view cine sequences  $\{x_t^{2CH}, x_t^{3CH}, x_t^{4CH}, x_t^{SAX}\}_{t=1}^T$ , the U-Net generates pixel-wise chamber segmentation masks  $\{S_t\}_{t=1}^T$  that explicitly delineate anatomical boundaries. The optimization of U-Net is supervised using Dice score loss between predicted and manually labeled cardiac regions:

$$\mathcal{L}_{U-Net} = 1 - Dice(S_t, \hat{S}_t). \quad (1)$$

The obtained anatomical feature embeddings  $\mathbf{z}_t^{\text{anatomy}}$  from different views can be fused as the cardiac anatomical representation for downstream image-mesh mapping.

For mesh feature extraction, we use a pretrained mesh VAE to learn a comprehensive prior over both cardiac geometry and temporal dynamics. Each 4D mesh sequence  $\{M_t\}_{t=1}^T$  is represented as a sequence of spatial graphs  $\mathcal{G}_t = (\mathcal{V}_t, \mathcal{E})$ , where  $\mathcal{V}_t$  denotes time-dependent vertex coordinates and  $\mathcal{E}$  denotes fixed mesh connectivity. The mesh VAE employs a hierarchical encoder-decoder architecture, as presented in Fig. 1 (b). A spatial graph convolutional network (GCN) branch captures local geometric structure, while a parallel graph attention branch, implemented via Exphormer (Shirzad et al., 2023), models long-range dependencies. The outputs of these branches are fused through a residual skip connection. The encoder comprises a series of mesh feature extraction blocks, each followed by downsampling to progressively reduce spatial resolution while expanding feature dimensions. Fixed downsampling matrices ( $\mathbf{D}_m$ ), precomputed on the atlas surface mesh using the method in Ranjan et al. (2018), transition among different resolution levels. At the bottleneck, the encoder maps the input mesh at time step  $t$  to parameters of a latent Gaussian distribution, i.e.,  $\mathbf{z}_t^{\text{mesh}}$ . The decoder mirrors this architecture, using upsampling matrices ( $\mathbf{U}_m$ ) to reconstruct the mesh from the latent sample. The mesh VAE is optimized by minimizing:

$$\mathcal{L}_{\text{MeshVAE}} = \frac{1}{T} \sum_{t=1}^T \left\| M_t - \hat{M}_t \right\|^2 + \lambda_{KL} \mathcal{R}_{KL}, \quad (2)$$

where  $M_t$  and  $\hat{M}_t$  represent the input and reconstructed mesh at time  $t$ , and  $\mathcal{R}_{KL}$  is the Kullback-Leibler (KL) divergence term.

The core of our approach is to learn an optimal mapping  $\mathcal{T}_{I \rightarrow M}$  between the anatomical embedding space  $\mathbf{z}^{\text{anatomy}}$  and the geometric embedding space  $\mathbf{z}^{\text{mesh}}$ . For efficient adaptation, we use low-rank adaptation (LoRA) (Hu et al., 2022) applied to the decoder of mesh VAE (see Sec. 3.4). This design enables personalized 4D mesh reconstruction by mapping segmentation-based anatomical features to geometrically plausible mesh sequences through the learned latent correspondence, while maintaining the rich geometric priors encoded in the frozen mesh VAE components.

### 3.2. Multi-Scale Latent Dynamics Modeling for Temporal Coherence

Modeling clinically meaningful cardiac function requires capturing both cycle-level temporal patterns (global feature) and short-term inter-frame consistency (local feature). To address this requirement, we propose a multi-scale temporal (MST) modeling module, as shown in Fig. 1 (d). This framework operates on fused anatomical embeddings and explicitly models temporal evolution at multiple scales. At each time step  $t$ , the anatomical latent embeddings  $\mathbf{z}_t^{\text{anatomy}}$  from multiple imaging views (LAX

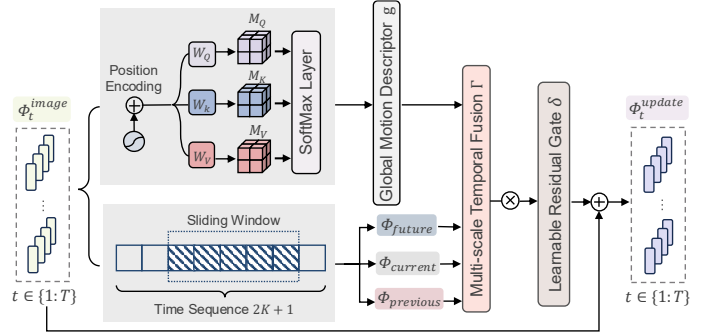


Figure 2: Multi-scale temporal modeling on the fused image features.

and SAX) are fused via a multi-view module consisting of fully-connected layers and linear projection, yielding a unified representation  $\Phi_t^{\text{image}}$ . To preserve temporal ordering, sinusoidal positional encoding (Vaswani et al., 2017) is added to the fused latent sequence.

As illustrated in Fig. 2, our temporal modeling architecture employs two complementary branches. A global branch applies temporal self-attention to the stacked latent embeddings, with pooled outputs yielding a global motion descriptor  $\mathbf{g}$  that encodes sequence-wide temporal context. Simultaneously, a local branch enforces short-term consistency among neighboring frames through a sliding window mechanism. For each reference frame  $t$ , neighboring frames within a temporal sliding window  $\mathcal{W}_t$  of total size  $(2K + 1)$  are grouped into three relative temporal categories: past frames  $\Phi_{\text{previous}} = \{\Phi_{t-j}^{\text{image}}\}_{j=1}^K$ , the current frame  $\Phi_{\text{current}} = \Phi_t^{\text{image}}$ , and future frames  $\Phi_{\text{future}} = \{\Phi_{t+j}^{\text{image}}\}_{j=1}^K$ . This grouping enables modeling of direction-aware temporal dependencies. We define  $\Gamma$  as a multi-scale fusion module that jointly leverages the global features  $\mathbf{g}$  and the local neighborhood window  $\mathcal{W}_t$  to produce a temporally informed latent representation. This is implemented by feature-space stacking of sequence-level and sliding-window context, fused by a compact projection head. The complete temporal update is formulated as:

$$\hat{\Phi}_t = \Gamma(\mathbf{g}, \mathcal{W}_t), \quad \Phi_t^{\text{update}} = \Phi_t^{\text{image}} + \delta \odot \hat{\Phi}_t, \quad (3)$$

where  $\delta$  is a learnable residual gating vector that controls the integration of temporal information into the geometry-aware latent state.

### 3.3. Differentiable Rendering for Contour-Guided Mesh Optimization

Multi-view cine MRI captures cardiac anatomy through sparse view-specific planes, providing complementary yet inherently 2D observations of a 3D heart. To reconstruct a complete 4D mesh under such planar supervision, we require a differentiable coupling that translates vertex-to-plane distances into continuous per-view contributions, enabling stable contour-driven mesh refinement. Our approach is motivated by the physical principle of exponential attenuation described in the Beer-Lambert law (May-

erhöfer et al., 2020), where transmitted light intensity diminishes exponentially with increasing path length through a medium. This provides a natural computational analogy: mesh vertices positioned near an imaging plane should exert stronger influence on the projected contour, while distant vertices contribute negligibly, with the influence decaying smoothly as distance increases.

As illustrated in Fig. 1 (c), for each anatomical view  $x \in \{2\text{CH}, 3\text{CH}, 4\text{CH}, \text{SAX}\}$ , we extract the affine transformation from the fixed image header to recover the view-plane geometry  $\Pi^x$  in world coordinates. The predicted surface-mesh vertices  $\hat{\mathbf{v}}_t^i$  at time frame  $t$  are represented in the same coordinate system, where  $i$  indexes individual mesh vertices. Each imaging plane  $\Pi^x$  is parameterized by a point  $\mathbf{c}^x$  lying on the plane and a unit normal vector  $\mathbf{n}^x$ , both defined in world coordinates. The perpendicular distance from a predicted vertex to this plane is computed as:

$$D_t^{i,x} = \text{dist}(\hat{\mathbf{v}}_t^i, \Pi^x) = |\mathbf{n}^x \cdot (\hat{\mathbf{v}}_t^i - \mathbf{c}^x)|. \quad (4)$$

Drawing upon the Beer-Lambert analogy, we transform these distances into plane-association probabilities  $p_t^{i,x}$  that quantify how strongly each vertex contributes to the projected view. A sigmoid-weighted distance function  $\ell_{\text{sigmoid}}(\cdot)$  combined with exponential attenuation yields:

$$p_t^{i,x} = 1 - \exp\left(-\mu \ell_{\text{sigmoid}}(D_t^{i,x})\right), \quad (5)$$

where  $\ell_{\text{sigmoid}}(D) = \sigma(\alpha(\tau - D))$  defines a decreasing proximity window with respect to the vertex-to-plane distance. Here,  $\alpha$  controls the steepness of the sigmoid transition,  $\tau$  determines the effective slab thickness around the imaging plane, and  $\mu$  controls the saturation strength of the exponential attenuation. Vertices close to the imaging plane therefore obtain higher association probabilities, whereas geometrically distant vertices are smoothly down-weighted. The sigmoid window provides a smooth differentiable transition around the imaging plane, while the exponential term controls how strongly this proximity response is converted into a plane-association probability. These vertex-wise probabilities are then projected onto their respective view planes and aggregated to construct probability maps  $P_t^x$ . This aggregation mechanism ensures that vertices in close proximity to the imaging plane contribute prominently, while geometrically distant vertices are progressively suppressed, naturally emphasizing the anatomical contours visible in each slice. The differentiable rendering (DR) objective is formulated as:

$$\mathcal{L}_{\text{DR}} = \sum_x \mathcal{L}_{\text{boundary}}(P_t^x, S_t^x), \quad (6)$$

where  $\mathcal{L}_{\text{boundary}}$  implements the boundary constraint proposed in Kervadec et al. (2019), and  $S_t^x$  represents the ground-truth segmentation mask for view  $x$  at time  $t$ . This loss is computed across all temporal frames, providing dense supervisory signals throughout the cardiac cycle. The boundary loss formulation is particularly appropriate here, as it operates on contour distances rather

than requiring pixel-wise classification, aligning naturally with our contour-based supervision paradigm.

### 3.4. Personalized Inference of 4D Whole-Heart Mesh

During inference, the image encoder  $f_e^I$  is kept frozen. The learned image-to-mesh mapping  $\mathcal{T}_{I \rightarrow M}$ , which encodes MST features, serves as a conditioning signal to the mesh decoder  $f_d^M$  for generating subject-specific, temporally coherent 4D whole-heart meshes. The generation process is formulated as:

$$\hat{M} = \text{LoRA}(f_d^M) \left( \mathcal{T}_{I \rightarrow M}(f_e^I(I)) \right), \quad (7)$$

where  $\text{LoRA}(\cdot)$  denotes the low-rank adaptation blocks integrated into the linear layers of the mesh decoder to enable parameter-efficient adaptation under a fixed backbone (Hu et al., 2022). The two modality-specific feature extractors ( $f^I$  for image and  $f^M$  for mesh) are trained independently. To ensure geometric regularity of the predicted surface, we employ an edge-length regularizer  $\mathcal{L}_{\text{edge}}$  and a normal-consistency regularizer  $\mathcal{L}_{\text{norm}}$ .  $\mathcal{L}_{\text{edge}}$  discourages abnormal stretching or shrinkage by penalizing variations in edge lengths, while  $\mathcal{L}_{\text{norm}}$  stabilizes local surface orientation by regularizing face normals (Wang et al., 2018). The reconstruction fidelity is measured by the mean squared error  $\mathcal{L}_{\text{MSE}}$  between the predicted mesh  $\hat{M}$  and the ground-truth mesh  $M$ . Combined with the regularizer  $\mathcal{L}_{\text{DR}}$  defined in Eq. (6), the total optimization objective is:

$$\mathcal{L}_{\text{total}} = \lambda_{\text{MSE}} \mathcal{L}_{\text{MSE}}(\hat{M}, M) + \lambda_{\text{DR}} \mathcal{L}_{\text{DR}} + \lambda_{\text{edge}} \mathcal{L}_{\text{edge}} + \lambda_{\text{norm}} \mathcal{L}_{\text{norm}}, \quad (8)$$

where  $\lambda_{\text{MSE}}$ ,  $\lambda_{\text{DR}}$ ,  $\lambda_{\text{edge}}$ , and  $\lambda_{\text{norm}}$  are weighting coefficients balancing the respective loss terms.

## 4. Experiments and Results

### 4.1. Data Acquisition and Pre-Processing

We collected 222 multi-view cine MRI scans from post myocardial infarction (MI) patients at the National University Hospital (NUH) in Singapore. Each patient has up to two sets of scans, with a time interval of approximately 6 months to 12 months. Specifically, the set includes a stack of SAX balanced steady-state free precession (bSSFP) cine MRI and three LAX cine sequences (2-, 3-, and 4-chamber views), acquired using Siemens 3T scanner. The SAX cine sequences consist of 7 to 14 slices across 25 frames. All images were cropped into a unified size of  $150 \times 150$  centering at the heart region, with intensity normalization via Z-score. The dataset was randomly divided into 155 training, 10 validation, and 67 test samples. To avoid data leakage, all data from a single patient were kept within the same data split (training, validation, or testing).

Table 1: Quantitative results of whole-heart and cardiac substructure mesh reconstruction. LV: left ventricle; RV: right ventricle; LA: left atrium; RA: right atrium; MAE: mean absolute error; MSE: mean squared error.

		Whole Heart	LV	RV	LA	RA
HybridVNet	MAE (mm) ↓	2.18 ± 0.54	1.70 ± 0.54	1.97 ± 0.55	2.31 ± 0.70	2.51 ± 0.60
	MSE (mm <sup>2</sup> ) ↓	8.80 ± 5.31	5.10 ± 3.67	7.02 ± 4.72	9.58 ± 9.24	11.72 ± 10.14
	$J_m$ (mm/frame <sup>3</sup> ) ↓	2.29 ± 0.23	1.73 ± 0.16	2.07 ± 0.15	2.27 ± 0.25	2.70 ± 0.28
Ours	MAE (mm) ↓	1.68 ± 0.31	1.59 ± 0.34	1.64 ± 0.35	1.99 ± 0.48	1.86 ± 0.58
	MSE (mm <sup>2</sup> ) ↓	5.06 ± 1.79	4.45 ± 1.93	4.86 ± 2.15	6.90 ± 3.19	6.26 ± 4.06
	$J_m$ (mm/frame <sup>3</sup> ) ↓	0.77 ± 0.17	0.69 ± 0.15	0.78 ± 0.17	0.91 ± 0.21	0.93 ± 0.23

Table 2: Summary of 2D contour results of predicted mesh on different views. DR: differentiable rendering; MCD: Mean Contour Distance; BF: Boundary F-score.

View	HybridVNet		Ours (w/o $\mathcal{L}_{DR}$ )		Ours	
	BF (%) ↑	MCD (mm) ↓	BF (%) ↑	MCD (mm) ↓	BF (%) ↑	MCD (mm) ↓
2CH	55.80 ± 12.05	2.85 ± 4.76	60.13 ± 9.89	2.30 ± 0.47	<b>65.47 ± 10.41</b>	<b>1.99 ± 0.41</b>
3CH	54.62 ± 9.01	3.60 ± 0.66	58.27 ± 9.31	2.32 ± 0.46	<b>65.71 ± 10.32</b>	<b>1.97 ± 0.44</b>
4CH	57.01 ± 9.14	3.69 ± 5.10	59.64 ± 8.68	2.42 ± 0.46	<b>68.24 ± 9.24</b>	<b>1.89 ± 0.38</b>
SAX	62.74 ± 13.56	2.22 ± 0.89	60.74 ± 11.53	2.29 ± 0.59	<b>62.86 ± 13.74</b>	<b>2.03 ± 0.62</b>

#### 4.2. Ground Truth and Evaluation Metrics

Cine MRI segmentation was first derived from an automated pipeline (Tasmurzayev et al., 2025) followed by manual refinement to ensure segmentation quality. The manual refinement was performed by a well-trained biomedical engineering student using ITK-SNAP and double checked by a senior expert. These refined segmentations were subsequently resampled into an aligned world coordinate system to form a sparse 3D volume, which is fed into the atlas-deformation process introduced by Xu et al. (2024) to produce a dense 3D segmentation label map. By leveraging the fixed affine correspondence between the volume space and the surface mesh vertices of atlas, the dense label map was projected onto a unified high-resolution template to generate topology-consistent whole-heart surface meshes. Each mesh consists 88,424 vertices and 176,828 faces and includes five anatomical components, namely LV, LV myocardium (Myo), right ventricle (RV), left atrium (LA), and right atrium (RA). This surface mesh was then served as the ground truth whole heart mesh.

For evaluation, we employed vertex-wise Mean Absolute Error (MAE) and Mean Squared Error (MSE) computed between the reference and predicted whole-heart surface meshes. Chamfer Distance (CD) and Hausdorff Distance (HD) were additionally reported for shape similarity assessment, and per-mesh inference time was measured for computational comparison. Furthermore, Mean Contour Distance (MCD) and boundary F-score (BF) were reported between the reference and predicted contours for each view, where MCD measures the average contour distance and BF quantifies boundary alignment (Cheng et al., 2019; Gur et al., 2019).  $E_{vol}$  was reported as the whole-heart volumetric error (mL), averaged over frames, using the absolute volume difference. Mesh jitter ( $J_m$ ) measured the temporal smoothness of vertex trajectories over time (Shin et al., 2024; Yi et al., 2022). For each 4D heart mesh data, chamber volumes were computed over time and the ejection fraction (EF) correlation has also been used as a

measurement.

#### 4.3. Implementation Details

The framework was implemented in PyTorch, running on a computer with a 13th Gen Intel(R) Core(TM) i9-13980HX CPU and an NVIDIA GeForce RTX 4090D GPU. We used the Adam optimizer to update the network parameters via stochastic gradient descent. The balancing parameters in Sec. 3.4 are set as follows:  $\lambda_{MSE} = 10$ ,  $\lambda_{DR} = 5$ ,  $\lambda_{edge} = 0.8$ , and  $\lambda_{norm} = 0.8$ . We pretrained the MeshVAE for 350 epochs using a learning rate of  $1 \times 10^{-4}$ . For image-mesh mapping, we trained the model for 400 epochs using the Adam optimizer with a learning rate of  $5 \times 10^{-5}$  and a batch size of 4. The temporal sliding window size is set to 5 with  $K = 2$ . The learning rate for LoRA applied to the pretrained mesh decoder is set to  $1e-5$ .

#### 4.4. Results of the Proposed Method

The proposed method obtained a promising result for reconstructing 4D whole heart from cine MRI, with an average MAE of  $1.68 \pm 0.31$  mm and MSE of  $5.06 \pm 1.79$  mm<sup>2</sup>. Besides the overall performance of the proposed model on the whole heart, we also analyzed its performance across all cardiac substructures, as presented in Table 1. One can see that compared to the baseline model, i.e., HybridVNet (Gaggion et al., 2025), our model consistently obtained better performance at both global and chamber-specific levels. Specifically, the left and right ventricles yield an average MAE of  $1.59 \pm 0.34$  mm and  $1.64 \pm 0.35$  mm, with corresponding MSE of  $4.45 \pm 1.93$  mm<sup>2</sup> and  $4.86 \pm 2.15$  mm<sup>2</sup>. For the left and right atria, average MAE are  $1.99 \pm 0.48$  mm and  $1.86 \pm 0.58$  mm, while average MSE are  $6.90 \pm 3.19$  mm<sup>2</sup> and  $6.26 \pm 4.06$  mm<sup>2</sup>, respectively. In general, we can observe that ventricular reconstructions achieved higher geometric accuracy than atrial reconstructions. This can be attributed to the fundamental asymmetry in cross-sectional sampling inherent

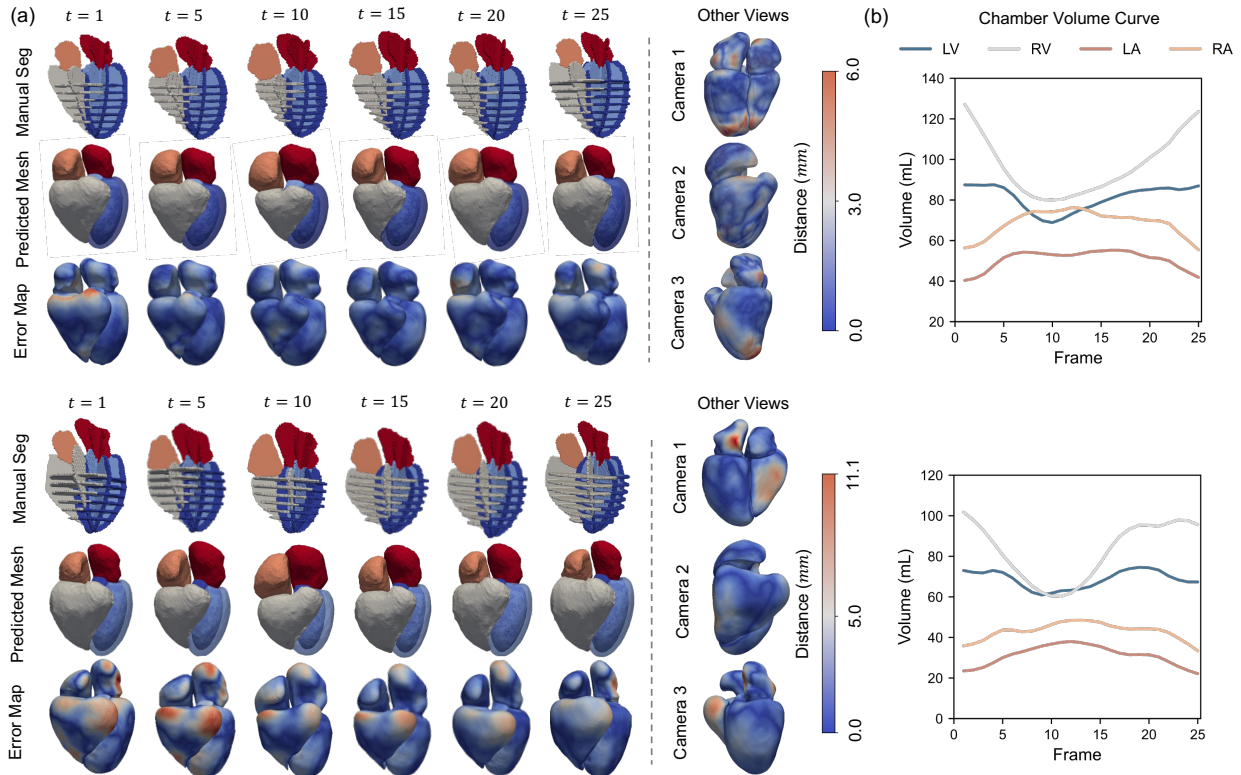


Figure 3: Illustration of whole-heart reconstruction quality of two representative cases. (a) Reconstructed 3D whole heart geometry at different cardiac phases and views. (b) Corresponding volume curves of reconstructed cardiac chambers.

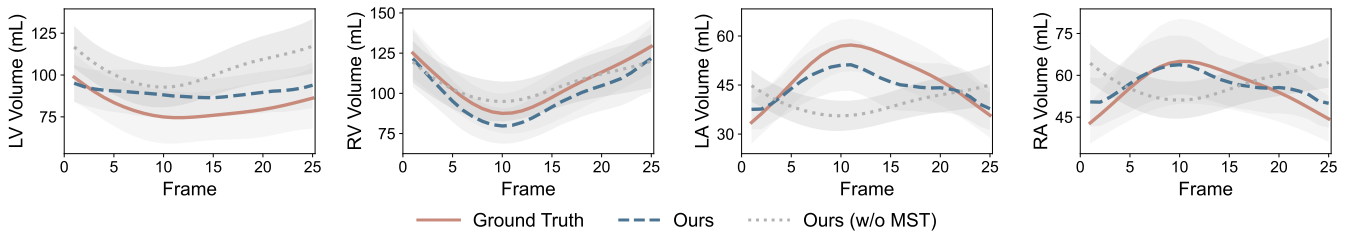


Figure 4: Illustration of chamber volume curves (mean  $\pm$  std) of ground truth and predicted whole heart mesh. MST: multi-scale temporal.

to standard multi-view cardiac MRI protocols. The ventricles are sampled through several short-axis stacks, providing multiple, spatially correlated 2D contours along the long-axis direction. In contrast, the atria are represented by only a single long-axis slice in each imaging plane, resulting in a substantially sparser set of cross-sectional observations. Consequently, the model has substantially more spatial information from which to infer the ventricular geometry, whereas atrial shape estimation must rely on far more limited and often incomplete anatomical evidence.

This sampling-induced performance disparity is further corroborated by our 2D contour alignment analysis across different imaging views, as summarized in Table 2. We observe that the SAX view, which comprises multiple slices along the ventricular long axis, achieves the lowest mean contour distance ( $2.03 \pm 0.62$  mm) among all views,

indicating superior geometric alignment precision. However, the SAX view yields a boundary F-score of  $62.86 \pm 13.74\%$ , which is slightly lower than those of the long-axis views (2CH:  $65.47 \pm 10.41\%$ , 3CH:  $65.71 \pm 10.32\%$ , 4CH:  $68.24 \pm 9.24\%$ ). This discrepancy can be explained by the inherent characteristics of each metric: mean contour distance measures the average Euclidean deviation between predicted and ground-truth contours, where SAX benefits from dense slice sampling that constrains the geometric solution space. In contrast, boundary F-score balances precision and recall, and the lower score of SAX view may reflect the increased complexity of matching multiple parallel slices, where small misalignments across the stack can accumulate and reduce the overall boundary overlap. The long-axis views, despite having sparser sampling, capture the chamber boundaries in a single sagittal plane, yielding higher boundary consistency at the expense of geomet-

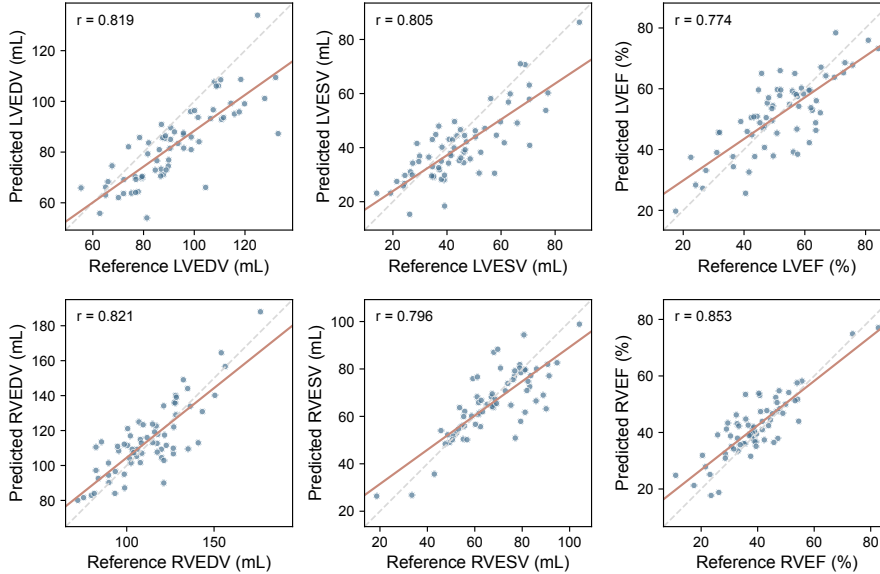


Figure 5: Correlation between predicted and reference ventricular functional indices. Pearson correlation coefficient ( $r$ ) is reported in each panel. Dashed grey lines indicate identity, and solid red lines indicate linear regression fits. LVEDV/ RVEDV: LV/ RV end-diastolic volume; LVESV/ RVESV: LV/ RV end-systolic volume; LVEF/ RVEF: LV/RV ejection fraction.

ric precision. These complementary observations collectively underscore the trade-offs inherent in multi-view reconstruction, where different imaging planes offer distinct strengths in capturing anatomical features.

Figure 3 shows qualitative reconstruction results for two representative cases with different performance levels. As shown in Fig. 3 (a), the proposed model reconstructed temporally coherent whole-heart meshes across the cardiac cycle from sparse cine MRI observations. In the first case, the predicted meshes closely followed the manual segmentations, with low surface errors across most cardiac structures and only minor local deviations near anatomically complex regions. In the second, more challenging case, larger errors were observed, particularly around the atrial and basal regions, reflecting the difficulty of recovering complete whole-heart anatomy from limited image evidence. Nevertheless, the reconstructed meshes remained anatomically plausible and temporally smooth across cardiac phases. The visualized error maps from additional viewpoints further indicated that the model preserved overall 3D structural consistency despite local reconstruction errors. Fig. 3 (b) presents the corresponding chamber volume curves calculated based on predicted mesh, where the predicted temporal volume changes exhibited physiologically reasonable trends over the cardiac cycle.

Figure 4 illustrates the temporal evolution of average chamber volumes derived from predicted and ground-truth meshes across the cardiac cycle. The predicted volumetric curves exhibit strong agreement with the ground truth in both magnitude and phase, demonstrating the ability of the proposed model to capture cardiac shape dynamics. However, the predicted LV volume change appears attenuated compared to the reference. This obser-

vation is consistent with the pathological profile of our cohort, which comprises exclusively post-MI patients. In such patients, infarcted myocardial segments exhibit little to no contractile function, leading to a characteristically blunted global LV volume variation. Modeling this altered, pathology-specific motion pattern presents a distinct challenge compared to modeling healthy cardiac dynamics. Notably, despite the inherent challenges posed by sparse cross-sectional sampling, the model successfully captures volume dynamics for the atrial chambers, which typically present greater reconstruction difficulty due to limited imaging evidence. We further examined the agreement between predicted and reference ventricular functional indices referring to Gaggion et al. (2025), as presented in Fig. 5. The reconstructed 4D whole-heart meshes achieved strong correlations for ventricular volumes, with  $r = 0.819$  for LV ED volume (LVEDV),  $r = 0.805$  for LV end-systolic volume (LVESV),  $r = 0.821$  for RV ED volume (RVEDV), and  $r = 0.796$  for RV ES volume (RVESV). Ejection fraction estimation also showed good agreement, with  $r = 0.774$  for LVEF and  $r = 0.853$  for RVEF. The relatively low LVEF and RVEF values observed in several cases are clinically plausible, as this is a post-MI cohort with potentially impaired ventricular contractility. Overall, these results indicate that the reconstructed 4D whole-heart meshes preserved clinically relevant volumetric dynamics and can provide reliable functional measurements.

#### 4.5. Comparison Study

We compare our method against representative point-based and mesh-based reconstruction approaches, with quantitative results summarized in Table 3. Among all methods, our proposed model achieved the lowest Chamfer dis-

Table 3: Summary of the quantitative evaluation results of 4D whole heart mesh reconstruction of different methods. Comparison results were reported in Chen et al. (2021) and Gaggion et al. (2025). CD: Chamfer distance; HD: Hausdorff distance.

Method	CD (mm) ↓	HD (mm) ↓	Inference Time (s) ↓
PointNet+ (Qi et al., 2017)	13.03 ± 2.96	17.04 ± 3.57	< 0.1
PU-Net (Yu et al., 2018)	12.15 ± 2.88	15.74 ± 3.37	< 0.1
Pixel2mesh (Wang et al., 2018)	19.38 ± 5.54	16.20 ± 3.30	< 0.1
CPD (Myronenko and Song, 2010)	12.10 ± 6.63	13.05 ± 7.04	37.45
GMMREG (Jian and Vemuri, 2010)	20.90 ± 7.18	18.57 ± 3.04	60.90
MR-Net (Chen et al., 2021)	4.39 ± 1.48	6.89 ± 1.88	< 0.1
HybridVNet (Gaggion et al., 2025)	4.13 ± 1.16	5.17 ± 1.02	< 0.1
<b>Ours</b>	<b>3.41 ± 0.62</b>	<b>5.13 ± 0.80</b>	< 0.1

tance ( $3.41 \pm 0.62$  mm) and Hausdorff distance ( $5.13 \pm 0.80$  mm), outperforming the previous state-of-the-art HybridVNet (Gaggion et al., 2025) by margins of 0.72 mm and 0.04 mm, respectively. Notably, while traditional registration methods such as CPD (Myronenko and Song, 2010) and GMMREG (Jian and Vemuri, 2010) require substantial computation time (up to 60.9 seconds per case), our method maintained real-time inference ( $< 0.1$  seconds) comparable to learning-based approaches. The superior performance of our method can be attributed to the synergistic integration of multi-view differentiable rendering and MST modeling, which together enforce both geometric precision and temporal coherence throughout the cardiac cycle.

We further analyze reconstruction performance across cardiac substructures and imaging views, as presented in Tables 1 and 2. Compared to HybridVNet, our method achieved consistent improvements across all chambers, with whole-heart MAE decreasing from  $2.18 \pm 0.54$  mm to  $1.68 \pm 0.31$  mm (23.0% reduction) and MSE from  $8.80 \pm 5.31$  mm<sup>2</sup> to  $5.06 \pm 1.79$  mm<sup>2</sup> (42.5% reduction). The temporal smoothness metric  $J_m$  also improves substantially from  $2.29 \pm 0.23$  to  $0.77 \pm 0.17$  mm/frame<sup>3</sup>, confirming that our multi-scale temporal modeling yields physiologically plausible motion. Ventricular reconstructions remained more accurate than atrial ones across both methods. The differentiable rendering loss yields the most pronounced gains in long-axis views (2CH, 3CH, 4CH), with boundary F-score improvements of 17.33%, 20.30%, and 19.70% relative to HybridVNet, respectively. These larger gains stem from the single-slice nature of long-axis views, where even small 3D deviations translate directly into contour misalignment, making direct boundary supervision particularly impactful. Qualitatively, the chamber volume curves in Fig. 4 demonstrated strong alignment with ground truth, capturing expected cardiac motion patterns and further validating the physiological consistency of our predictions.

#### 4.6. Ablation Study

We conduct ablation experiments to evaluate the contribution of each core component in our framework, with quantitative results presented in Table 4. The full model achieves the lowest MSE ( $5.06 \pm 1.79$  mm<sup>2</sup>), MAE ( $1.68 \pm 0.31$  mm), and volumetric error  $E_{vol}$  ( $17.3 \pm 11.2\%$ ),

Table 4: Quantitative results of ablation studies evaluating different components of the proposed method for the 4D whole heart reconstruction. VAE: variational autoencoder; MST: multi-scale temporal.

Method	MSE ↓	MAE ↓	$E_{vol}$ ↓
w/o SAX	5.64 ± 2.00	1.76 ± 0.31	25.3 ± 10.6
w/o 2CH	5.59 ± 1.94	1.72 ± 0.29	27.3 ± 12.8
w/o 3CH	5.87 ± 1.96	1.80 ± 0.30	25.3 ± 11.7
w/o 4CH	5.99 ± 1.91	1.82 ± 0.28	26.3 ± 9.8
w/o U-Net	6.43 ± 1.94	1.87 ± 0.28	30.8 ± 14.5
w/o VAE	5.67 ± 2.03	1.77 ± 0.32	25.0 ± 10.8
w/o MST	5.32 ± 2.02	1.69 ± 0.29	24.7 ± 13.0
<b>Ours</b>	<b>5.06 ± 1.79</b>	<b>1.68 ± 0.31</b>	<b>17.3 ± 11.2</b>

demonstrating the synergistic effect of all components. Multi-view feature fusion proves essential for accurate reconstruction. Removing any single view increases reconstruction error, with the 4CH view being most critical (MSE increases to  $5.99 \pm 1.91$  mm<sup>2</sup>), as it simultaneously captures all four chambers and provides comprehensive anatomical context. The SAX view contributes through-plane resolution critical for ventricular geometry, while long-axis views capture apical and longitudinal anatomy, together enabling complete 3D reconstruction. This confirms that complementary information from all imaging planes is necessary for accurate whole-heart modeling. Geometric priors from MeshVAE pretraining (w/o VAE) increase MSE to  $5.67 \pm 2.03$  mm<sup>2</sup> and substantially degrade volumetric error ( $25.0 \pm 10.8\%$  versus  $17.3 \pm 11.2\%$  for the full model), indicating that constraining reconstructions to a plausible anatomical manifold benefits both spatial accuracy and temporal consistency. Segmentation-based pretraining via U-Net (w/o U-Net) yields the largest performance drop among all components (MSE:  $6.43 \pm 1.94$  mm<sup>2</sup>), as anatomical boundary features learned during segmentation provide critical edge-specific information for accurate mesh-image alignment, outperforming intensity-based self-supervision.

The multi-scale temporal modeling block (w/o MST) increases MSE to  $5.32 \pm 2.02$  mm<sup>2</sup> and volumetric error to  $24.7 \pm 13.0\%$ , highlighting its importance for temporal coherence. This effect is further substantiated by the chamber volume curves presented in Fig. 4. The full model closely tracks the ground-truth volume trajectory throughout the cardiac cycle, accurately capturing both the magnitude and phase of chamber contraction and relaxation. In contrast, the variant without multi-scale temporal mod-

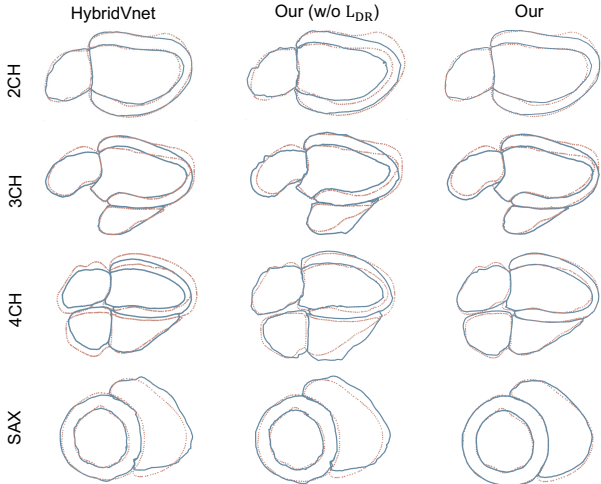


Figure 6: Qualitative comparison of multi-view contour alignment, where dash lines indicate ground truth and solid lines refer to estimated contours of different methods.

eling (w/o MST) exhibits attenuated volume changes and phase misalignment, particularly at end-systole, indicating that the absence of global-local temporal fusion leads to oversmoothed motion dynamics. These results confirm that the MST design, which jointly leverages sequence-level global motion and inter-frame consistency, is essential for modeling physiologically plausible cardiac motion.

The DR loss  $\mathcal{L}_{DR}$  plays a critical role in enforcing contour alignment across imaging planes. As shown in Table 2, removing  $\mathcal{L}_{DR}$  (ours w/o DR) degrades boundary F-scores across all views, with the largest impact on long-axis views (2CH: from 65.47% to 60.13%; 3CH: from 65.71% to 58.27%; 4CH: from 68.24% to 59.64%). These gains are visually confirmed in Fig. 6, where the full model achieved precise contour overlap with ground-truth segmentations, whereas the variant without DR exhibits noticeable misalignments, particularly in regions with complex anatomy. This demonstrates that while vertex-wise MSE minimizes global distances, it does not penalize misalignment against specific 2D cuts, a limitation that  $\mathcal{L}_{DR}$  explicitly addresses by rendering and comparing against 2D segmentations.

#### 4.7. External Validation on the Public Cine MRI Dataset

To assess the generalization capability of the proposed 4D whole-heart mesh reconstruction framework, we conducted external validation on the public CMR-MULTI-Fused cine MRI dataset released with the BAAI Cardiac Agent study (Qu et al., 2026). This dataset contains 105 cardiac MRI data collected under multi-center and missing-view (3CH view is not available) settings, thereby providing a challenging test bed for evaluating model robustness beyond the internal training distribution. We compared HybridVNet, the proposed model without LoRA adaptation, and the proposed model using both geometric reconstruction errors and temporal motion consistency metrics. Table 5 presents the quantitative results on the external

Table 5: Performance on the external dataset for 4D whole-heart mesh reconstruction.

Metric	HybridVNet	Ours (w/o LoRA)	Ours
CD (mm) ↓	<b>4.88 ± 1.96</b>	5.41 ± 0.17	4.98 ± 0.26
HD (mm) ↓	<b>15.46 ± 3.67</b>	17.33 ± 0.84	16.33 ± 0.96
MAE (mm) ↓	4.82 ± 1.04	3.44 ± 0.34	<b>2.69 ± 0.39</b>
MSE (mm <sup>2</sup> ) ↓	25.61 ± 5.05	20.33 ± 3.87	<b>12.99 ± 3.91</b>
$J_m$ (mm/frame <sup>3</sup> ) ↓	2.90 ± 1.12	1.94 ± 1.02	<b>1.82 ± 1.88</b>

cine MRI dataset. LoRA adaptation consistently improved the proposed model across all evaluation metrics, reducing CD from 5.41 mm to 4.98 mm, HD from 17.33 mm to 16.33 mm, MAE from 3.44 mm to 2.69 mm, MSE from 20.33 mm<sup>2</sup> to 12.99 mm<sup>2</sup>, and motion jitter  $J_m$  from 1.94 to 1.82 mm/frame<sup>3</sup>. Compared with HybridVNet, the proposed model achieved substantially lower MAE, MSE, and  $J_m$ , indicating improved point-wise reconstruction accuracy and temporal motion consistency. HybridVNet obtained slightly lower CD and HD, suggesting competitive global surface proximity; however, its higher point-wise errors and motion jitter indicate less accurate mesh correspondence and less stable temporal dynamics. Overall, these results demonstrate that the proposed framework generalizes effectively to external cine MRI data and that LoRA-based adaptation further improves robustness under cross-dataset distribution shift.

#### 4.8. Proof-of-Concept In-Silico Electrophysiological Simulation

To assess whether the reconstructed anatomy can support downstream computational modeling, we performed whole-heart EP simulation on a representative case. The reconstructed surface mesh was first converted into an upsampled volumetric mesh using the InSilicoHeartGen pipeline, where Cobiveco local coordinates, ventricular fibre orientation, and anatomy-specific anisotropy were assigned (Doste et al., 2026; Schuler et al., 2021). The atria were modelled with isotropic conduction. For the ventricles, a simplified His-Purkinje system was incorporated by defining seven early activation sites, following Gerach et al. (2023), together with a thin fast-conducting subendocardial layer whose conduction velocity was set to twice that of the surrounding myocardium. Both the His-Purkinje root locations and the subendocardial layer were defined in Cobiveco local coordinates (Gillette et al., 2021), while atrial activation sites were manually specified. EP propagation was simulated using the monodomain model implemented in openCARP (Plank et al., 2021). The atria and ventricles were treated as separate physical regions with different ionic models: the Courtemanche model for the atria and the Ten Tusscher-Panfilov model for the ventricles. To approximate atrioventricular conduction delay, ventricular stimulation was initiated 200 ms after atrial stimulation. The torso was approximated as an infinite homogeneous volume conductor, from which a simulated ECG signal was computed. As shown in Fig. 7, the simulation reproduced the expected sequence of atrial depolar-

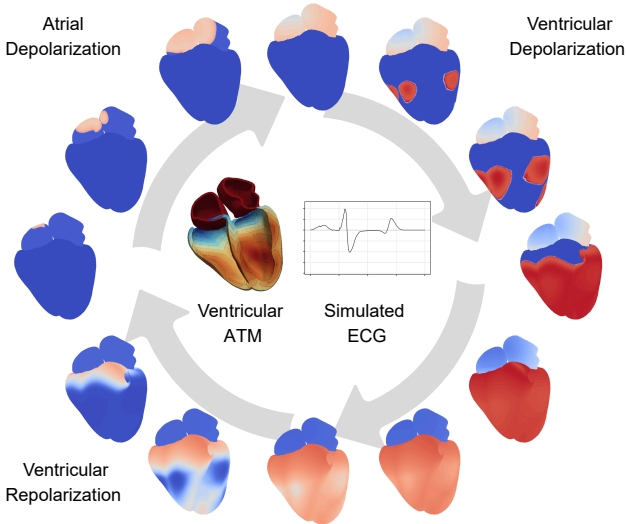


Figure 7: Whole-heart electrophysiological simulation over one cardiac cycle. The outer sequence shows transmembrane-potential propagation during atrial depolarization, ventricular depolarization, and ventricular repolarization. The center shows the ventricular activation-time map (ATM) and the simulated ECG.

ization, ventricular depolarization, and ventricular repolarization, together with a physiologically plausible ventricular activation-time map and ECG waveform. The ventricular activation pattern was qualitatively consistent with classical experimental observations (Durrer et al., 1970). Although the current simulation uses generic EP parameters without subject-specific personalization or regional action-potential-duration heterogeneity, this proof-of-concept experiment suggests that the reconstructed whole-heart mesh can be converted into a simulation-ready anatomical substrate for downstream EP modeling.

## 5. Discussion and Conclusion

In this study, we have presented a fully automatic end-to-end framework for personalized 4D whole-heart mesh reconstruction from sparse multi-view 2D cine MRI. The proposed model achieved superior geometric accuracy compared to state-of-the-art methods, as demonstrated in Tables 1 and 3. This performance gain can be attributed to three key contributions. First, the differentiable rendering loss grounded in the Beer-Lambert law enables anatomy-aware supervision from sparse 2D segmentations. As shown in Table 2 and Fig. 6, removing this loss (ours w/o DR) substantially degraded boundary F-scores, particularly in long-axis views, confirming that vertex-wise MSE alone cannot enforce alignment against specific 2D cuts. Second, the MST modeling block, which fuses global cycle-level context with local inter-frame consistency, proved essential for physiologically plausible motion. The ablation study (Table 4) shows that removing this block (w/o MST) increased volumetric error, and Fig. 4 further illustrates that the full model closely tracks ground-truth

volume trajectories while the w/o MST variant exhibits attenuated contraction and phase misalignment. Third, unlike prior works that focus narrowly on biventricular myocardium (Yuan et al., 2023; Laumer et al., 2025), our method reconstructs complete four-chamber meshes. Notably, we observed that ventricular reconstructions consistently outperformed atrial ones, which we attribute to the fundamental sampling asymmetry in standard multi-view protocols: ventricles benefit from dense short-axis stacks while atria rely on only a single long-axis slice per view (see Section 4.4). This disparity was further corroborated by the 2D contour analysis in Table 2, where SAX views achieved the lowest mean contour distance due to dense sampling constraints. Finally, the proof-of-concept in-silico EP simulation (Section 4.8) suggests that the reconstructed whole-heart meshes can serve as simulation-ready anatomical substrates, supporting the feasibility of using routine cine MRI for future CDT modeling.

Nevertheless, three limitations of this work should be acknowledged. First, our method relies on accurate 2D segmentations from cine MRI as supervision. While we employed an automated pipeline with manual refinement, segmentation errors can propagate to the reconstructed meshes. As shown in Table 2, the boundary F-scores for long-axis views remain lower than ideal, reflecting residual segmentation uncertainty. Second, the current framework reconstructs whole-heart geometry but does not incorporate tissue property estimation (e.g., myocardial stiffness, conductivity) or biomechanical constraints, which are essential for downstream EP or electromechanical simulations. Third, our method has only been tested on post-MI patients. While this cohort represents a clinically relevant population with diverse infarct patterns, the generalizability to other pathologies (e.g., cardiomyopathy, valvular disease, atrial fibrillation) and to healthy subjects remains to be validated. Additionally, as shown in Fig. 4, the predicted LV volume change appeared attenuated compared to ground truth. The reduced LV volume variation in the predicted curves may reflect the difficulty of modeling subtle, pathology-altered contraction patterns in post-MI patients. Although post-MI physiology is characterized by impaired contractility, the remaining discrepancy with the reference curves indicates that further improvement is needed for accurately capturing motion amplitude.

In our future work, we plan to address these limitations and extend the framework toward a fully integrated CDT platform. First, we will incorporate self-supervised or weakly supervised learning strategies to reduce dependence on manual segmentations. Second, we aim to integrate biomechanical priors into the reconstruction pipeline, enabling direct estimation of tissue properties and patient-specific electromechanical parameters from the same sparse cine MRI inputs. Third, we will evaluate the proposed method on a larger multi-center population across different scanner vendors, imaging protocols, and disease cohorts (including healthy controls) to thoroughly investigate its generalization ability. On this

larger dataset, we can perform a comprehensive sensitivity analysis to quantitatively investigate the impact of sampling variability and slice misalignment on reconstruction accuracy. Fourth, we plan to extend the temporal modeling to handle variable-length and arrhythmic cycles using sequence-to-sequence models or neural ordinary differential equations, broadening clinical applicability to patients with rhythm disorders. Additionally, we will explore a more detailed patient-specific whole-heart-torso modeling framework, incorporating cardiac motion and distinct anatomical compartments (atria, ventricles, great vessels, pericardium) to enhance the fidelity of downstream simulations. Finally, we will work toward an end-to-end training scheme that jointly optimizes segmentation, reconstruction, and temporal modeling, potentially via differentiable graph networks or implicit neural representations, to further streamline the pipeline and reduce error propagation. In conclusion, this work demonstrates the feasibility of automatic 4D whole-heart mesh reconstruction from routine clinical cine MRI, achieving both geometric accuracy and temporal coherence, paving the way for future research to enable large-scale, real-time CDT applications.

## References

- Arevalo, H.J., Vadakkumpadan, F., Guallar, E., Jebb, A., Malamas, P., Wu, K.C., Trayanova, N.A., 2016. Arrhythmia risk stratification of patients after myocardial infarction using personalized heart models. *Nature Communications* 7, 11437.
- Banerjee, A., Camps, J., Zacur, E., Andrews, C.M., Rudy, Y., Choudhury, R.P., Rodriguez, B., Grau, V., 2021. A completely automated pipeline for 3D reconstruction of human heart from 2D cine magnetic resonance slices. *Philosophical Transactions of the Royal Society A* 379, 20200257.
- Beetz, M., Banerjee, A., Grau, V., 2021. Biventricular surface reconstruction from cine mri contours using point completion networks, in: 2021 IEEE 18th International Symposium on Biomedical Imaging (ISBI), IEEE. pp. 105–109.
- Beetz, M., Banerjee, A., Grau, V., 2024. Modeling 3d cardiac contraction and relaxation with point cloud deformation networks. *IEEE Journal of Biomedical and Health Informatics* 28, 4810–4819.
- Beetz, M., Banerjee, A., Ossenberg-Engels, J., Grau, V., 2023. Multi-class point cloud completion networks for 3d cardiac anatomy reconstruction from cine magnetic resonance images. *Medical image analysis* 90, 102975.
- Bello, G.A., Dawes, T.J., Duan, J., Biffi, C., De Marvao, A., Howard, L.S., Gibbs, J.S.R., Wilkins, M.R., Cook, S.A., Rueckert, D., et al., 2019. Deep-learning cardiac motion analysis for human survival prediction. *Nature machine intelligence* 1, 95–104.
- Bistoquet, A., Oshinski, J., Škrinjar, O., 2008. Myocardial deformation recovery from cine mri using a nearly incompressible biventricular model. *Medical image analysis* 12, 69–85.
- Boyle, P.M., Zghaib, T., Zahid, S., Ali, R.L., Deng, D., Franceschi, W.H., Hakim, J.B., Murphy, M.J., Prakosa, A., Zimmerman, S.L., et al., 2019. Computationally guided personalized targeted ablation of persistent atrial fibrillation. *Nature biomedical engineering* 3, 870–879.
- Bransby, K.M., Tufaro, V., Cap, M., Slabaugh, G., Bourantas, C., Zhang, Q., 2023. 3d coronary vessel reconstruction from bi-plane angiography using graph convolutional networks, in: 2023 IEEE 20th International Symposium on Biomedical Imaging (ISBI), IEEE. pp. 1–5.
- Chen, X., Ravikumar, N., Xia, Y., Attar, R., Diaz-Pinto, A., Piechnik, S.K., Neubauer, S., Petersen, S.E., Frangi, A.F., 2021. Shape registration with learned deformations for 3d shape reconstruction from sparse and incomplete point clouds. *Medical image analysis* 74, 102228.
- Cheng, D., Liao, R., Fidler, S., Urtasun, R., 2019. Darnet: Deep active ray network for building segmentation, in: Proceedings of the IEEE/CVF conference on computer vision and pattern recognition, pp. 7431–7439.
- Chong, B., Jayabaskaran, J., Jauhari, S.M., Chan, S.P., Goh, R., Kueh, M.T.W., Li, H., Chin, Y.H., Kong, G., Anand, V.V., et al., 2025. Global burden of cardiovascular diseases: projections from 2025 to 2050. *European journal of preventive cardiology* 32, 1001–1015.
- Corral-Acero, J., Margara, F., Marciniak, M., Rodero, C., Loncaric, F., Feng, Y., Gilbert, A., Fernandes, J.F., Bukhari, H.A., Wajdan, A., et al., 2020. The ‘digital twin’ to enable the vision of precision cardiology. *European heart journal* 41, 4556–4564.
- Doste, R., Camps, J., Wang, Z.J., Berg, L.A., Holmes, M., Smith, H., Beetz, M., Li, L., Banerjee, A., Grau, V., et al., 2026. An automated computational pipeline for generating large-scale cohorts of patient-specific ventricular models in electromechanical in silico trials. *Computer Methods and Programs in Biomedicine* , 109290.
- Durrer, D., Van Dam, R.T., Freud, G., Janse, M.J., Meijler, F.L., Arzbaecher, R.C., 1970. Total excitation of the isolated human heart. *Circulation* 41, 899–912.
- Evain, E., Sun, Y., Faraz, K., Garcia, D., Saloux, E., Gerber, B.L., De Craene, M., Bernard, O., 2022. Motion estimation by deep learning in 2d echocardiography: Synthetic dataset and validation. *IEEE transactions on medical imaging* 41, 1911–1924.
- Fedele, M., Piersanti, R., Regazzoni, F., Salvador, M., Africa, P.C., Bucelli, M., Zingaro, A., Quarteroni, A., et al., 2023. A comprehensive and biophysically detailed computational model of the whole human heart electromechanics. *Computer Methods in Applied Mechanics and Engineering* 410, 115983.
- Gaggion, N., Matheson, B.A., Xia, Y., Bonazzola, R., Ravikumar, N., Taylor, Z.A., Milone, D.H., Frangi, A.F., Ferrante, E., 2025. Multi-view hybrid graph convolutional network for volume-to-mesh reconstruction in cardiovascular mri. *Medical Image Analysis* , 103630.
- Gerach, T., Schuler, S., Wachter, A., Loewe, A., 2023. The impact of standard ablation strategies for atrial fibrillation on cardiovascular performance in a four-chamber heart model. *Cardiovascular Engineering and Technology* 14, 296–314.
- Gillette, K., Gsell, M.A., Prassl, A.J., Karabelas, E., Reiter, U., Reiter, G., Grandits, T., Payer, C., Štern, D., Urschler, M., et al., 2021. A framework for the generation of digital twins of cardiac electrophysiology from clinical 12-lead ecgs. *Medical image analysis* 71, 102080.
- Gillette, K., Gsell, M.A., Stocchi, M., Grandits, T., Neic, A., Manning, M., Scherr, D., Roney, C.H., Prassl, A.J., Augustin, C.M., et al., 2022. A personalized real-time virtual model of whole heart electrophysiology. *Frontiers in Physiology* 13, 907190.
- Gur, S., Shaharabany, T., Wolf, L., 2019. End to end trainable active contours via differentiable rendering. *arXiv preprint arXiv:1912.00367* .
- Hu, E.J., Shen, Y., Wallis, P., Allen-Zhu, Z., Li, Y., Wang, S., Wang, L., Chen, W., et al., 2022. Lora: Low-rank adaptation of large language models. *ICLR* 1, 3.
- Hu, H., Pan, N., Frangi, A.F., 2023. Fully automatic initialization and segmentation of left and right ventricles for large-scale cardiac MRI using a deeply supervised network and 3d-ASM. *Computer Methods and Programs in Biomedicine* 240, 107679.
- Jian, B., Vemuri, B.C., 2010. Robust point set registration using gaussian mixture models. *IEEE transactions on pattern analysis and machine intelligence* 33, 1633–1645.
- Joyce, T., Buoso, S., Stoock, C.T., Kozerke, S., 2022. Rapid inference of personalised left-ventricular meshes by deformation-based differentiable mesh voxelization. *Medical image analysis* 79, 102445.
- Kervadec, H., Bouchtiba, J., Desrosiers, C., Granger, E., Dolz, J., Ayed, I.B., 2019. Boundary loss for highly unbalanced segmentation, in: International conference on medical imaging with deep learning, PMLR. pp. 285–296.

- Kong, F., Shadden, S.C., 2022. Learning whole heart mesh generation from patient images for computational simulations. *IEEE Transactions on Medical Imaging* 42, 533–545.
- Laumer, F., Rubi, L., Matter, M.A., Buoso, S., Fringeli, G., Mach, F., Ruschitzka, F., Buhmann, J.M., Matter, C.M., 2025. 2d echocardiography video to 3d heart shape reconstruction for clinical application. *Medical Image Analysis* 101, 103434.
- Lemeunier, C., Denis, F., Lavoué, G., Dupont, F., 2022. Representation learning of 3d meshes using an autoencoder in the spectral domain. *Computers & Graphics* 107, 131–143.
- Li, L., Camps, J., Rodriguez, B., Grau, V., 2024a. Solving the inverse problem of electrocardiography for cardiac digital twins: A survey. *IEEE Reviews in Biomedical Engineering*.
- Li, L., Camps, J., Wang, Z., Beetz, M., Banerjee, A., Rodriguez, B., Grau, V., 2024b. Towards enabling cardiac digital twins of myocardial infarction using deep computational models for inverse inference. *IEEE Transactions on Medical Imaging*.
- Li, L., Smith, H., Lyu, Y., Camps, J., Qian, S., Rodriguez, B., Banerjee, A., Grau, V., 2025. Personalized topology-informed localization of standard 12-lead ecg electrode placement from incomplete cardiac mris for efficient cardiac digital twins. *Medical Image Analysis* 101, 103472.
- Liu, X., Yuan, X., Chan, M.Y., Sia, C.H., Li, L., 2026. Cinemesh4d: Personalized 4d whole heart reconstruction from sparse cine mri. *arXiv preprint arXiv:2605.13994*.
- López, P.A., Mella, H., Uribe, S., Hurtado, D.E., Costabal, F.S., 2023. Warppinn: Cine-mr image registration with physics-informed neural networks. *Medical Image Analysis* 89, 102925.
- Lyu, Y., Chan, M.Y., Sia, C.H., Li, L., 2026. Personalized 3d myocardial infarct geometry reconstruction from cine mri for cardiac digital twins. *arXiv preprint arXiv:2606.01808*.
- Ma, Q., Meng, Q., Qiao, M., Matthews, P.M., O'Regan, D.P., Bai, W., 2026. Cardiac mesh flow: One-step generation of 3d+ t cardiac four-chamber meshes via flow matching. *arXiv preprint arXiv:2605.01884*.
- Ma, Q., Meng, Q., Qiao, M., Matthews, P.M., O'Regan, D.P., Bai, W., 2025. Cardiacflow: 3d+ t four-chamber cardiac shape completion and generation via flow matching, in: *International Conference on Medical Image Computing and Computer-Assisted Intervention*, Springer. pp. 89–99.
- Mayerhöfer, T.G., Pahlow, S., Popp, J., 2020. The bouguer-beer-lambert law: Shining light on the obscure. *ChemPhysChem* 21, 2029–2046.
- Meng, Q., Bai, W., Liu, T., O'regan, D.P., Rueckert, D., 2022. Mesh-based 3d motion tracking in cardiac mri using deep learning, in: *International conference on medical image computing and computer-assisted intervention*, Springer. pp. 248–258.
- Meng, Q., Bai, W., O'Regan, D.P., Rueckert, D., 2023. Deepmesh: Mesh-based cardiac motion tracking using deep learning. *IEEE transactions on medical imaging* 43, 1489–1500.
- Myronenko, A., Song, X., 2010. Point set registration: Coherent point drift. *IEEE transactions on pattern analysis and machine intelligence* 32, 2262–2275.
- Odille, F., Bustin, A., Liu, S., Chen, B., Vuissoz, P.A., Felblinger, J., Bonnemains, L., 2018. Isotropic 3D cardiac cine MRI allows efficient sparse segmentation strategies based on 3D surface reconstruction. *Magnetic resonance in medicine* 79, 2665–2675.
- Oktay, O., Ferrante, E., Kamnitsas, K., Heinrich, M., Bai, W., Caballero, J., Cook, S.A., De Marvao, A., Dawes, T., O'Regan, D.P., et al., 2017. Anatomically constrained neural networks (acnns): application to cardiac image enhancement and segmentation. *IEEE transactions on medical imaging* 37, 384–395.
- Ouyang, D., He, B., Ghorbani, A., Yuan, N., Ebinger, J., Langlotz, C.P., Heidenreich, P.A., Harrington, R.A., Liang, D.H., Ashley, E.A., et al., 2020. Video-based ai for beat-to-beat assessment of cardiac function. *Nature* 580, 252–256.
- Plank, G., Loewe, A., Neic, A., Augustin, C., Huang, Y.L., Gsell, M.A., Karabelas, E., Nothstein, M., Prassl, A.J., Sánchez, J., et al., 2021. The opencarp simulation environment for biomedic electrophysiology. *Computer Methods and Programs in Biomedicine* 208, 106223.
- Qi, C.R., Yi, L., Su, H., Guibas, L.J., 2017. Pointnet++: Deep hierarchical feature learning on point sets in a metric space. *Advances in neural information processing systems* 30.
- Qiao, M., Wang, Y., Guo, Y., Huang, L., Xia, L., Tao, Q., 2020. Temporally coherent cardiac motion tracking from cine mri: Traditional registration method and modern cnn method. *Medical Physics* 47, 4189–4198.
- Qu, T., Zhang, H., Zhang, L., Zhao, C., Zhang, N., Wang, H., Zhou, Z., Zou, M., Bo, K., Zhao, P., et al., 2026. Baai cardiac agent: An intelligent multimodal agent for automated reasoning and diagnosis of cardiovascular diseases from cardiac magnetic resonance imaging. *arXiv preprint arXiv:2604.04078*.
- Ranjan, A., Bolkart, T., Sanyal, S., Black, M.J., 2018. Generating 3d faces using convolutional mesh autoencoders, in: *Proceedings of the European conference on computer vision (ECCV)*, pp. 704–720.
- Ronneberger, O., Fischer, P., Brox, T., 2015. U-net: Convolutional networks for biomedical image segmentation, in: *International Conference on Medical image computing and computer-assisted intervention*, Springer. pp. 234–241.
- Salvador, M., Strocchi, M., Regazzoni, F., Augustin, C.M., Dede', L., Niederer, S.A., Quarteroni, A., 2024. Whole-heart electromechanical simulations using latent neural ordinary differential equations. *NPJ Digital Medicine* 7, 90.
- Sarmah, M., Neelima, A., Singh, H.R., 2023. Survey of methods and principles in three-dimensional reconstruction from two-dimensional medical images. *Visual computing for industry, biomedicine, and art* 6, 15.
- Schuler, S., Pilia, N., Potyagaylo, D., Loewe, A., 2021. Cobiveco: Consistent biventricular coordinates for precise and intuitive description of position in the heart—with matlab implementation. *Medical Image Analysis* 74, 102247.
- Shin, S., Kim, J., Halilaj, E., Black, M.J., 2024. Wham: Reconstructing world-grounded humans with accurate 3D motion, in: *Proceedings of the IEEE/CVF Conference on Computer Vision and Pattern Recognition*, pp. 2070–2080.
- Shirzad, H., Vellingker, A., Venkatachalam, B., Sutherland, D.J., Sinop, A.K., 2023. Expformer: Sparse transformers for graphs, in: *International Conference on Machine Learning*, PMLR. pp. 31613–31632.
- Tasmurzayev, N., Amangeldy, B., Imanbek, B., Baigarayeva, Z., Imankulov, T., Dikhanbayeva, G., Amangeldi, I., Sharipova, S., 2025. Digital cardiovascular twins, ai agents, and sensor data: A narrative review from system architecture to proactive heart health. *Sensors* 25, 5272.
- Ukwatta, E., Arevalo, H., Li, K., Yuan, J., Qiu, W., Malamas, P., Wu, K.C., Trayanova, N.A., Vadakkumpadan, F., 2015. Myocardial infarct segmentation from magnetic resonance images for personalized modeling of cardiac electrophysiology. *IEEE Transactions on Medical Imaging* 35, 1408–1419.
- Vaswani, A., Shazeer, N., Parmar, N., Uszkoreit, J., Jones, L., Gomez, A.N., Kaiser, L., Polosukhin, I., 2017. Attention is all you need. *Advances in neural information processing systems* 30.
- Villard, B., Grau, V., Zacur, E., 2018. Surface mesh reconstruction from cardiac MRI contours. *Journal of Imaging* 4, 16.
- Wang, L., Clarysse, P., Liu, Z., Gao, B., Liu, W., Croisille, P., Delachartre, P., 2019. A gradient-based optical-flow cardiac motion estimation method for cine and tagged mr images. *Medical image analysis* 57, 136–148.
- Wang, N., Zhang, Y., Li, Z., Fu, Y., Liu, W., Jiang, Y.G., 2018. Pixel2mesh: Generating 3d mesh models from single rgb images, in: *Proceedings of the European conference on computer vision (ECCV)*, pp. 52–67.
- Xiao, J., Zheng, W., Wang, W., Xia, Q., Yan, Z., Guo, Q., Wang, X., Nie, S., Zhang, S., 2024. Slice2mesh: 3d surface reconstruction from sparse slices of images for the left ventricle. *IEEE Transactions on Medical Imaging* 44, 1541–1555.
- Xu, H., Muffoletto, M., Niederer, S.A., Williams, S.E., Williams, M.C., Young, A.A., 2023. Whole heart 3d shape reconstruction from sparse views: leveraging cardiac computed tomography for cardiovascular magnetic resonance, in: *International Conference*

- on Functional Imaging and Modeling of the Heart, Springer. pp. 255–264.
- Xu, Y., Xu, H., Sinclair, M., Puyol-Antón, E., Niederer, S.A., Chiribiri, A., Williams, S.E., Williams, M.C., Young, A.A., 2024. Improved 3d whole heart geometry from sparse cmr slices, in: International Workshop on Statistical Atlases and Computational Models of the Heart, Springer. pp. 43–52.
- Yang, X., Yuan, X., Li, H., Chen, L., Liu, Y., Li, L., 2026. Repcm: Region-specific and phenotype-adaptive bi-ventricular cardiac motion synthesis. arXiv preprint arXiv:2605.21237 .
- Ye, M., Yang, D., Kanski, M., Axel, L., Metaxas, D., 2023. Neural deformable models for 3d bi-ventricular heart shape reconstruction and modeling from 2d sparse cardiac magnetic resonance imaging, in: Proceedings of the IEEE/CVF International Conference on Computer Vision, pp. 14247–14256.
- Yi, X., Zhou, Y., Habermann, M., Shimada, S., Golyanik, V., Theobalt, C., Xu, F., 2022. Physical inertial poser (pip): Physics-aware real-time human motion tracking from sparse inertial sensors, in: Proceedings of the IEEE/CVF conference on computer vision and pattern recognition, pp. 13167–13178.
- Yu, J., Duan, Y., Huang, Y., Wang, Y., Ling, R., Luo, W., Zhang, A., Xu, J., Ni, Q., Zhou, Y., et al., 2025. Ultratwin: towards cardiac anatomical twin generation from multi-view 2d ultrasound, in: International Conference on Medical Image Computing and Computer-Assisted Intervention, Springer. pp. 608–617.
- Yu, L., Li, X., Fu, C.W., Cohen-Or, D., Heng, P.A., 2018. Pu-net: Point cloud upsampling network, in: Proceedings of the IEEE conference on computer vision and pattern recognition, pp. 2790–2799.
- Yu, Y., Zhang, S., Li, K., Metaxas, D., Axel, L., 2014. Deformable models with sparsity constraints for cardiac motion analysis. *Medical image analysis* 18, 927–937.
- Yuan, X., Liu, C., Wang, Y., 2023. 4d myocardium reconstruction with decoupled motion and shape model, in: Proceedings of the IEEE/CVF International Conference on Computer Vision, pp. 21252–21262.
- Zappon, E., Azzolin, L., Gsell, M.A., Thaler, F., Prassl, A.J., Arnold, R., Gillette, K., Kariman, M., Manninger, M., Scherr, D., et al., 2025. An efficient end-to-end computational framework for the generation of eeg calibrated volumetric models of human atrial electrophysiology. *Medical image analysis* , 103822.
- Zheng, Q., Delingette, H., Ayache, N., 2019. Explainable cardiac pathology classification on cine mri with motion characterization by semi-supervised learning of apparent flow. *Medical image analysis* 56, 80–95.